第 3 4 卷第 10 期　　焊　接　学　报　　Vol. 34　No. 10
2 0 1 3 年 1 0 月　　TRANSACTIONS OF THE CHINA WELDING INSTITUTION　　October　2 0 1 3

薄板铝合金激光深熔焊熔池流动数值模拟

占小红[1,2]，　米高阳[1]，　陶　汪[3]，　陈　洁[2]，　魏艳红[1,3]，　陈彦宾[3]

(1. 南京航空航天大学 材料科学与技术学院，南京　210016; 2. 中国商飞上海飞机制造有限公司，上海　200436;
3. 哈尔滨工业大学 现代焊接生产技术国家重点实验室，哈尔滨　150001)

占小红

摘　要: 针对薄板铝合金激光焊接过程,采用有限体积法开展熔池流动研究. 建立了三维焊接熔池流动数学模型,并采用高斯旋转体热源表征激光束的热作用. 在考虑与不考虑表面张力作用下,分别计算获得了焊接温度场、熔池流场和熔池形貌. 基于计算结果,分析了温度场云纹图、熔池焊接热循环曲线、熔池速度场分布多视图. 最后进行相同参数下的激光焊接试验,基于观察获得的焊接接头形貌,综合分析了模拟结果和试验结果. 结果表明,所建立的模型和模拟方法是合理可行的. 同时考虑 Marangoni 对流作用所计算得到的熔池和焊缝几何形状更加接近实际焊接接头.

关键词: 铝合金; 激光焊; 熔池; 流场

中图分类号: TG402　　**文献标识码**: A　　**文章编号**: 0253 - 360X(2013)10 - 0031 - 04

0　序　　言

激光焊是一个涉及传质、传热、冶金和力学的复杂过程,其熔池的流动行为极为复杂. 与传统的熔焊相比,由于匙孔的存在,激光深熔焊接熔池液体的流动更加复杂. 随着计算机数值模拟技术的发展,采用数值模拟方法计算得到其熔池形状、熔池温度场、流场等指标,能够为评价并控制焊接质量提供重要依据. 国内外诸多研究人员针对激光深熔焊温度场及熔池流体流动展开了研究.

Andrews 等人[1] 建立了激光深熔焊三维模型,研究了熔池内的流动情况. Dowden[2] 采用交错网格技术对未穿透激光焊接传热过程进行研究,分别在粘度为常数和粘度随温度变化的情况下研究了小孔周围液态金属的流动. Solana 等人[3] 所建立的三维模型通过求解能量方程和压力方程,确定了未穿透激光焊接熔池形貌,计算中所有的边界通过计算获得而不是事先假定. 陈磊[4] 运用焓 - 孔隙度方法建立了移动热源作用下激光焊接过程的控制方程组,基于 PHOENICS 软件及其二次开发,模拟了浮力、表面张力、反蒸发力单独作用及联合作用下不锈钢大功率激光焊接的温度场和流场. 吴冰等人[5] 考虑了表面张力、浮力、液—固相之间内作用力、焊接速度、紊流、对流以及辐射等影响因素,建立激光深熔焊接过程运动熔池的数学模型,并对熔池的温度、流动、焊缝形貌的动态演化过程进行模拟预测. 此外张林杰[6]、李永强[7] 等人针对铝合金激光焊接过程气体流场、温度场等不同方面开展了建模与仿真研究.

常规材料、厚板、穿透焊的研究较为成熟. 然而新型铝合金薄板未穿透激光焊接过程中,更易产生气孔等缺陷. 为此有必要针对薄板铝合金未穿透激光深熔焊接过程温度场和流场进行研究. 采用高斯旋转体热源模型,分别考虑重力、表面张力、浮力等的作用,采用有限体积法进行求解计算,获得激光深熔焊温度场和熔池流场结果,对结果进行分析,并与实际焊缝进行比对,验证模拟的准确性.

1　控制方程和边界条件

1.1　控制方程

为了能够有效近似地考察激光深熔焊接过程熔池内液体流动,除需考虑了浮力、电磁力及表面张力对熔池内液体的驱动作用,还作如下假设. (1) 焊接过程为准稳态过程; (2) 熔池内的液体为牛顿不可压缩流体,流动方式为层流,固相不运动; (3) 忽略熔池表面波动; (4) 固相不变形且无内应力存在; (5) 热物理性能参数按常数处理.

激光深熔焊过程涉及匙孔内气态、熔池液态以

收稿日期: 2013 - 05 - 14

基金项目: 国家商用飞机制造工程技术研究中心创新基金资助项目 (SAMC12-JS-15-009); 国家自然科学基金资助项目 (51175253)

及被焊件固态的相互作用. 综合考虑多方因素,基于一定的假设,建立了包括连续性方程、能量方程和动量方程的控制方程组.

连续性方程为

$$\frac{\partial \rho}{\partial t} + \nabla(\rho u_i) = 0 \tag{1}$$

动量方程为

$$\frac{\partial(\rho u_i)}{\partial t} + \nabla(\rho u_i u_j) = \nabla(\mu \nabla u_i) + \frac{\mu}{K}(u_i - v) + S_{ui} \tag{2}$$

能量方程为

$$\frac{\partial(\rho h)}{\partial t} + \nabla(\rho u_i h) = \nabla\left(\frac{k}{c_p}\nabla h\right) + S_h \tag{3}$$

式中: ρ 为密度; u_i, u_j 为熔融金属在 x, y, z 方向速度; k 为热导率; v 为焊接速度; c_p 为定压比热容; h 为焓; μ 为粘度; S_h 为能量方程源项; S_{ui} 为动量方程源项.

动量方程的源项主要包括熔池液固两相混合区的多孔渗流作用以及浮力作用,其中浮力作用只作用在 z 方向上. x, y 方向动量方程源项为

$$S_{ui} = -\nabla p - C\left[\frac{(1-f_1)^2}{f_1^3 + B}\right]u_i \tag{4}$$

z 方向上的动量方程源项为

$$S_{ui} = -\frac{\partial p}{\partial z} - C\left[\frac{(1-f_1)^2}{f_1^3 + B}\right]w + \rho\beta g(T - T_s) \tag{5}$$

式中: p 为压力; f_1 为液态体积分数; B 为避免分母为零的很小的正数; C 为经验常数; β 为液体热膨胀系数; g 为重力加速度; T 为构件实际温度; T_s 为固相线温度.

能量方程的源项主要考虑了熔化过程中相变潜热和外加热源的作用,即

$$S_h = -\frac{\partial(\rho \Delta H)}{\partial t} - \nabla(\rho u_i \Delta H) + q(x,y,z) \tag{6}$$

式中: H 为相变潜热; $q(x,y,z)$ 为点 (x,y,z) 处的热流密度.

1.2 边界条件

激光深熔焊接过程中,焊缝形貌呈现具有较大深宽比的“钉头”状. 为了更准确的描述匙孔的加热作用,采用了高斯旋转体热源模型对激光热源进行表征,在直角坐标系下,高斯旋转体热源模型的数学表达式为

$$q(x,y,z) = \frac{3c_s Q}{\pi H(1-\mathrm{e}^{-3})}\exp\left[\frac{-3c_s}{\log\left(\frac{H_0}{z}\right)}(x^2+y^2)\right] \tag{7}$$

式中: H_0 为体热源的高度; Q 为激光束的有效功率; c_s 为热源形状集中系数.

焊件在上表面除焊接热源的热输入外,还存在着焊件与周围环境的对流换热和辐射换热,即

$$-k\mathrm{Grad}T = -q(x,y,z) + h_c(T - T_0) + k_b\varepsilon(T^4 - T_0^4) \tag{8}$$

式中: h_c 为对流换热系数; T_0 为环境温度; ε 为黑度系数; k_b 为波尔兹曼常数.

在上表面,除了对流辐射换热之外,液体还受到了表面张力的作用,即

$$\begin{aligned} -\mu\frac{\partial u}{\partial z} &= \frac{\partial \sigma}{\partial T}\frac{\partial T}{\partial x} \\ -\mu\frac{\partial v}{\partial z} &= \frac{\partial \sigma}{\partial T}\frac{\partial T}{\partial y} \end{aligned} \tag{9}$$

式中: σ 为表面张力; σ/T 为表面张力温度系数.

在其它各表面上,只有对流换热和辐射换热这两种形式,可表示为

$$-k\mathrm{Grad}T = h_c(T - T_0) + \sigma\varepsilon(T^4 - T_0^4) \tag{10}$$

2 焊接模型建立

建立了尺寸为 16 mm × 16 mm × 2 mm 的几何模型,对模型进行网格划分,靠近激光焊接热源区域进行网格细化,共建立了 32 000 个六面体单元和 8 280 个四边形面单元,如图 1 所示.

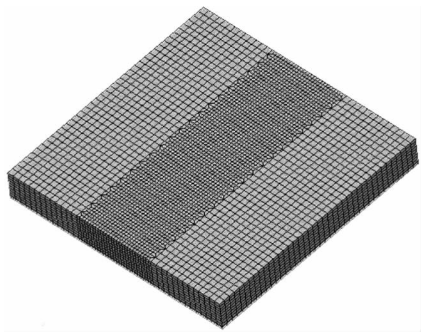

图 1 铝合金激光束焊接模型网格划分

Fig. 1 Mesh of laser beam welding model of aluminum alloys

计算选用的焊接参数为激光束垂直于工件表面入射,激光束有效功率为 1.5 kW,焊接速度为 0.02 m/s.

某新型铝合金的物理性能参数如表 1 所示. 将热源、边界条件、初始条件导入焊接模型,采用 simple 算法进行求解.

3 模拟结果分析

分别计算了纯传热作用下(不考虑 Marangoni

表 1　所用铝合金热物理性能参数

Table 1　Aluminum alloy thermophysical parameters

固相密度 ρ_s/(kg•m^{-3})	液相密度 ρ_l/(kg•m^{-3})	定压比热容 c_p/(J•kg•K^{-1})	固相热导率 k_s/(W•m^{-1}•K^{-1})	熔化潜热 L_m/(kJ•kg^{-1})	粘度系数 μ/(g•m^{-1}•s^{-1})
2 720	2 400	1 020	104.881	387	0.017 2
表面张力系数梯度 $d\sigma/dT$	**固相线温度 T_s/K**	**液相线温度 T_l/K**	**环境温度 T_0/K**	**重力加速度 g/(m•s^{-2})**	
-0.35×10^{-3}	904	1 014	300	9.81	

力) 和考虑负 Marangoni 力作用下薄板激光焊熔池的温度场和流场.

图 2a 为纯传热作用下的温度场分布. x-y 平面上由于移动热源的作用,熔池有明显的拖尾现象. 温度场分布呈长椭圆状,熔池前端温度梯度大于后部温度梯度. 图 2b 为考虑了负 Marangoni 力下的温度场分布. 相比纯传热作用下温度场,熔池拖尾较短,熔池表面宽度增加,焊缝形状呈“钉头状”. 移动热源中心熔池温度最高. 工件温度分布与所施加的高斯旋转体热源相符合.

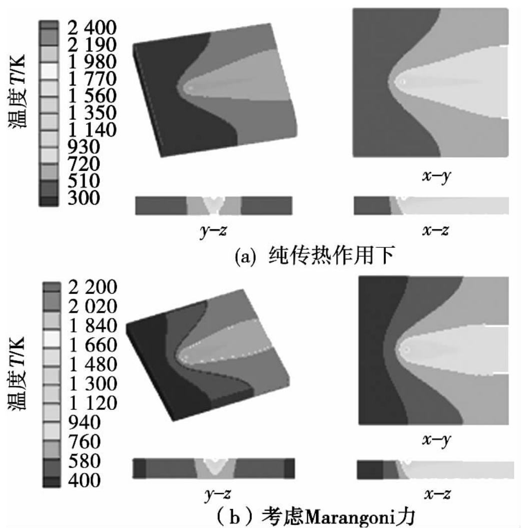

图 2　温度场分布图

Fig. 2　Distribution of temperature field

图 3a 为焊接前进方向的热循环分布曲线,从图 3 中可以看出,移动热源前端温度梯度明显大于移动热源后方的温度梯度. 在纯传热作用下,工件的峰值温度约为 2 300 K; 而考虑了负 Marangoni 力作用后,工件的峰值温度约为 2 100 K. 从图 3b 中可以看出工件的焊接温度分布沿纵截面(x-z 平面)对称. 结合图 3b 与图 3c 可得,考虑 Marangoni 力作用下的热循环曲线相对较平缓,纯导热作用下热循环曲线的斜率较大. 其原因是 Marangoni 力加快了熔池表面和垂直方向的熔池流动,熔池内的热量传输加快.

图 4 为负 Marangoni 力作用下熔池流动速度的矢量分布. 由 y-z 截面图可以得到,熔池中心处形成两个涡流. 在熔池上表面,熔融金属由熔池中心处流向熔池边缘,在靠近熔池中心处近似垂直向上流动. 到表面的距离增加时,流动速度减缓. 这是由于铝合金表面张力梯度为负值时,熔池边缘附近的温度较低,其表面张力较大; 而熔池中心温度较高,

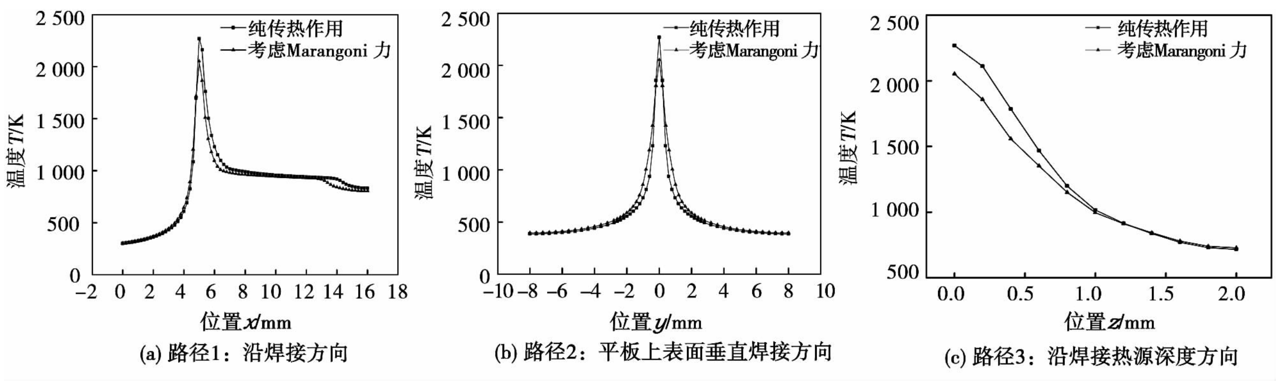

图 3　热循环曲线图

Fig. 3　Thermal cycle curve

其表面张力较小,导致熔融金属从熔池中心向熔池四周流动.

针对薄板铝合金进行激光焊试验,采用与模拟相同的参数进行试验,从图 5 可得,模拟结果与试验

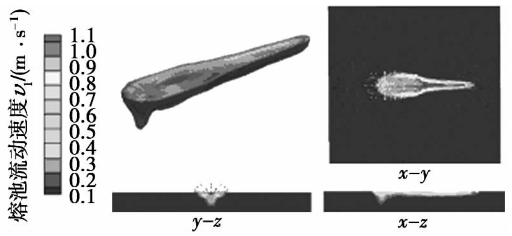

图 4 熔池速度分布图
Fig. 4 Velocity profile of molten pool

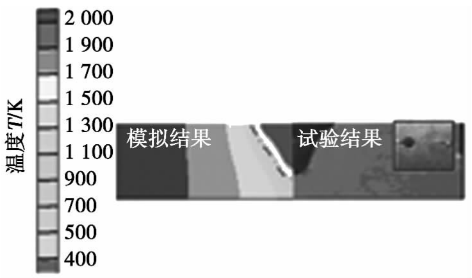

图 5 模拟焊缝几何形状与实际焊缝对比
Fig. 5 Comparison of simulated weld geometry and actual weld

结果吻合良好,验证了模拟结果的正确性.

4 结 论

(1) 为了准确描述激光深熔焊的特点,采用高斯旋转体热源表征激光热源的作用,并分别建立了纯传热作用和考虑 Marangoni 力作用下的焊接数学模型.

(2) 分别在纯传热作用下和在考虑 Marangoni 力作用下进行温度场模拟. 纯传热作用下获得的熔池最高温度较高. Marangoni 对流作用是影响熔池流动的主要驱动力之一,加强了焊接熔池的热传导和熔池流动速度.

(3) 在 Marangoni 力作用下获得了“钉头状”的焊缝形貌. 考虑 Marangoni 对流作用计算得到的熔池和焊缝几何形状更加接近实际焊接接头.

参考文献:

[1] Andrews J G, Atthey D R. Hydrodynamic limit to penetration of a material by a high-power beam[J]. Journal of Physics D: Applied Physics, 1976, 9: 2181 −2194.

[2] Dowden J. Interaction of the keyhole and weld pool in laser keyhole welding[J]. Journal of Laser Applications, 2002, 14(4): 204 −209.

[3] Solana P, Negro G. A study of effect of multi-reflections on the shape of the keyhole in laser processing of materials[J]. Journal of Physics D, 1997, 30(23): 3216 −3222.

[4] 陈 磊. 大功率激光焊接熔池特性数值模拟[D]. 兰州: 兰州理工大学, 2008.

[5] 吴 冰, 巩水利, 庞胜勇, 等. 激光深熔焊运动熔池瞬态形成过程数值模拟[J]. 焊接学报, 2010, 31(10): 1 −4.
Wu Bing, Gong Shuili, Pang Shengyong, *et al*. Numerical simulation of transient evolvement of molten pool in laser deep penetration welding[J]. Transactions of the China Welding Institution, 2010, 31(10): 1 −4.

[6] 张林杰, 张建勋, 段爱琴. 侧吹辅助气流对激光深熔焊接光致等离子体的影响[J]. 焊接学报, 2006, 27(10): 37 −40.
Zhang Linjie, Zhang Jianxun, Duan Aiqin. Effect of side gas on laser induced plasma during laser deep penetration welding[J]. Transactions of the China Welding Institution, 2006, 27(10): 37 −40.

[7] 李永强, 赵 贺, 赵熹华, 等. 铝合金 LB-RSW 焊接中 RSW 温度场的数值模拟[J]. 焊接学报, 2009, 30(4): 29 −32.
Li Yongqiang, Zhao He, Zhao Xihua, *et al*. Numerical simulation of RSW temperature field during aluminum alloys LB-RSW[J]. Transactions of the China Welding Institution, 2009, 30(4): 29 −32.

作者简介: 占小红,男,1979 年出生,博士,副教授. 主要从事焊接过程数值模拟及仿真、焊接工程软件、航空航天先进制造工艺等研究工作. 发表论文 20 余篇. Email: xhzhan@nuaa.edu.cn

Key words: mobile welding robot; seam tracking; dynamics; variable structure control with sliding mode

Corrosion behavior of high frequency resistance welding joint of Q125 grade tube steel under CO_2/H_2S environment

WU Huibin[1], LIU Lifu[1], WANG Lidong[2], TANG Di[1] (1. National Engineering Research Center of Advanced Rolling, University of Science and Technology Beijing, Beijing 100083, China; 2. AVIC Beijing Aeronautical Manufacturing Technology Research Institute, Beijing 100024, China). pp 17 – 21

Abstract: The corrosion behavior of high frequency resistance welding (ERW) joint of Q125 grade tube steel was studied by SEM, EBSD and electrochemical measurement under CO_2/H_2S environment. The results showed that the corrosion prosperty of joint was worse than that of the base metal and heat affected zone, thus the grooving corrosion occurred in the ERW welding joint under CO_2/H_2S environment. The proportion of large-angle grain boundary in welding zone was more than that of base metal and heat affected zone, which played an important role in the highest corrosion rate of welding zone. Electrochemical analysis results demonstrated that welding zone was easy to corrode because of its smallest polarization resistance in electrode reaction, while the polarization resistance of base metal was the biggest. All of these were consistent with the result of corrosion test and analysis of polarization curve.

Key words: welding joint; grooving corrosion; CO_2/H_2S corrosion; large-angle grain boundary

Effect of nano-CeO_2 on structure and properties of high velocity flame spraying coating

GUO Hongjian[1], LIANG Bunü[1], JIA Junhong[2], ZHANG Zhenyu[1] (1. Department of Mechanical Engineering, Lanzhou Institute of Technology, Lanzhou 730050, China; 2. State Key Laboratory of Solid Faubrication, Lanzhou Institute of Chemical Physics, Chinese Academy of Sciences, Lanzhou 730000, China). pp 22 – 26

Abstract: Different amount of nano-CeO_2 powder was added into NiCrFe/WC for spray. The coating was produced on Q235 substrate by CP-3000 high velocity flame spraying equipment. The microstructure and surface morphology of the coating were analyzed by optical microscopy and scanning electron microscopy. The phase composition of the coating was determined by X-ray diffraction. The wear properties of the coating were investigated by an M-200-wear-tester. The adhesive strength of the coating were investigated on an SHT4605 universal testing machine. The micro-hardness of the coating was evaluated by HXD-1000TM micro-hardness instrument. The results showed that nano-CeO_2 powder could refine the microstructure of the coating and improve the compactness of the coating, which also promoted the chemical metallurgical reaction among components in the process of solidification and crystallization of the coating. In the process of formation of the coating, some new phases were formed, such as NiCrFe、γ(Fe, Ni) solid solution and $CeNi_3$. These new phases improved the mechanical properties of the coating through solid solution strengthening. The micro-hardness, adhesive strength and wear resistance of the coating were greatly improved. The optimal addition of nano-CeO_2 powder was 1%.

Key words: nano-CeO_2 powder; high velocity flame spraying; coating; microstructure; mechanical property

Microstructure and mechanical properties of welding joints of X100 line pipe by double-wire submerged arc welding

LI Jihong, YANG Liang, CHEN Feichou, ZHNANG Min (College of Material Science and Engineering, Xi'an University of Technology, Xi'an 710048, China). pp 27 – 30

Abstract: The microstructure and mechanical properties of X100 pipeline steel were investigated by optical electron microscope, scanning electron microscope and material testing machine. The results indicate that the microstructure of X100 line pipe is mainly composed of acicular ferrite and granular bainite in weld zones. The polygon ferrite exists in HAZ and the grains are coarser, which lead to softening and embrittlement. The fusion line is clear between outer weld and inner weld. The tensile strength and elongation rate of the welded joint are up to the 805 MPa and 10.7%, respectively. The impact energy is more than 110 J, and the average percent of shear fracture gets to 85% at −10 ℃, which is ductile fracture. The results of hardness test show that the hardness of the HAZ of outer weld is higher than that of inner weld.

Key words: X100 line pipe; double-wire submerged arc welding; microstructure; mechanical properties

Molten flow simulation of laser deep penetration welding of aluminum alloys

ZHAN Xiaohong[1,2], MI Gaoyang[1], TAO Wang[3], CHEN Jie[2], WEI Yanhong[2,3], CHEN Yanbin[3] (1. College of Material Science and Technology, Nanjing University of Aeronautics and Astronautics, Nanjing 210016, China; 2. Shanghai Aircraft Manufacturing Co., Ltd, Shanghai 200436, China; 3. State Key Laboratory of Advanced Welding and Joining, Harbin Institute of Technology, Harbin 150001, China). pp 31 – 34

Abstract: A study on fluid flow in the molten pool of laser deep penetration welding process was carried out which utilized the finite volume method. A three dimensional fluid flow model was established and the effect of the laser beam was represented by the Gaussian rotating body heat source. The temperature field, fluid flow and weld shape were calculated considering the Marangoni effect. The temperature field contours, the welding thermal cycle curve of molten pool and the velocity field of molten pool were analyzed based on the calculated results. Finally, the laser welding experiment was carried out with the same weld parameters. The actual weld shape was observed. The simulation results and experiment results were comprehensively analyzed. The accuracy of the numerical simulation results was verified. The calculated geometries of the molten pool and welds were more similar to that of the experimental results when the Marangoni convection was considered.

Key words: aluminum; laser beam welding; welding pool; temperature field; fluid flow

Refill friction spot welding process for aluminium-lithium alloy

FENG Xiaosong[1], ZHANG Chengcong[1], GUO Lijie[2], MIAO Yugang[2] (1. Shanghai Aerospace Equipments Manufacturer, Shanghai 200245, China; 2. College of Shipbuilding Engi-